Simulation of External Hypersonic Problems Using FLUENT 6.3 Density-Based Coupled Solver

K. A. Kurbatskii, R. Kumar** and D. Mann****
** ANSYS - Fluent Inc.*
10 Cavendish Court, Lebanon, New Hampshire, USA
*** ANSYS - Fluent India Pvt Ltd.*
Plot No. 34/1, Pune Infotech Park, MIDC, Hinjewadi, Pune - 411057, India
**** Fluent Europe Ltd.*
Sheffield Business Park, 6 Europa View, Sheffield S9 1XH, United Kingdom

Abstract
Effective and robust numerical approach to external hypersonic problems using the general purpose CFD code FLUENT, version 6.3 is presented. Density-based coupled solver with second-order upwind discretization and AUSM+ flux splitting method is chosen. Flows with strong thermo-chemical effects are modeled using the laminar finite-rate chemistry model, otherwise the ideal gas approximation is applied. Both laminar and turbulent regimes are considered depending on the Reynolds number. SST k-ω turbulence model is employed as a baseline model. Near-wall region is resolved all the way to the laminar sublayer. Several benchmark cases are considered, and favorable agreements with experimental data are found.

1. Introduction

The accurate numerical prediction of external hypersonic flows can be a valuable tool in the evaluation of designs of atmospheric reentry systems, orbital transport ships, missiles and other flight vehicles operating at hypersonic speeds. The problem of hypersonic flows is complicated by the presence of shock discontinuities that can significantly affect vehicle control systems. It is essential for the analysis to accurately capture the shock location and to resolve the shock - boundary layer interaction. Simulation of external hypersonic aerodynamics becomes even more challenging at high hypersonic speeds when real-gas thermodynamic non-equilibrium processes become non-negligible and chemical dissociation of the gas has to be taken into account. Hypersonic aerodynamics has been studied computationally in recent years using specialized numerical methods[1-3]. This study presents an effective and robust numerical approach to external hypersonic problems using the general purpose CFD code FLUENT[4], version 6.3. Several benchmark cases including hypersonic flow over a sphere, hyperboloid flare, and a 3D hypersonic aerospike-protected missile are considered. Numerical results for pressure and thermal loads are compared with experimental data, and favorable agreements are found.

2. Numerical method

Steady-state numerical simulations are carried out using the general purpose CFD code FLUENT, version 6.3. The density-based coupled double-precision solver[4] is employed as a baseline solver. The governing equations for the conservation of mass, momentum and energy are discretized using a control-volume-based technique. The system of governing equations for a single-component fluid is cast in integral Cartesian form for an arbitrary control volume V with differential surface area $d\mathbf{A}$ as follows:

$$\frac{\partial}{\partial t}\int_V \mathbf{W}\,dV + \oint [\mathbf{F}-\mathbf{G}]\cdot d\mathbf{A} = \int_V \mathbf{H}\,dV \tag{1}$$

where the vectors **W**, **F** and **G** are defined as,

$$\mathbf{W} = \rho[1, u, v, w, E]^{\mathrm{T}},\ \mathbf{F} = [\rho\,\mathbf{v}, \rho\,\mathbf{v}\,u + p\,\hat{\mathbf{i}}, \rho\,\mathbf{v}\,v + p\,\hat{\mathbf{j}}, \rho\,\mathbf{v}\,w + p\,\hat{\mathbf{k}}, \rho\,\mathbf{v}\,E + p\,\mathbf{v}]^{\mathrm{T}},\ \mathbf{G} = [0, \tau_{xi}, \tau_{yi}, \tau_{zi}, \tau_{ij}\,v_j + \mathbf{q}]^{\mathrm{T}} \tag{2}$$

and the vector **H** contains source terms such as body forces and energy sources. Here ρ, **v**, E, and p are the density, velocity, total energy per unit mass, and pressure of the fluid, respectively, τ is the viscous stress tensor, and **q** is the heat flux. Total energy E is related to the total enthalpy H as $E = H - p / \rho$ where $H = h + |\mathbf{v}|^2/2$ and h is sensible enthalpy. The Navier-Stokes equations (1) become numerically very stiff at low Mach number due to the disparity between the fluid velocity and the acoustic speed of sound. The numerical stiffness of the equations under these conditions results in poor convergence rates. This difficulty is overcome by employing time-derivative preconditioning[5], which modifies the time-derivative term in (1) by pre-multiplying it with a preconditioning matrix. This has the effect of re-scaling the acoustic speed (eigenvalue) of the system of equations being solved in order to alleviate the numerical stiffness encountered in low Mach numbers and incompressible flow. Face values required for computing the convection terms are interpolated from the cell centers using the second-order upwind scheme[6]. Gradients needed for constructing values of a scalar at the cell faces and for computing secondary diffusion terms and velocity derivatives are calculated using the Green-Gauss node-based gradient evaluation[7]. In this approach, nodal values are constructed from the weighted average of the cell values surrounding the nodes, following the approach originally proposed by Holmes et al[8] and Rauch et al[9], and then gradients are computed at cell centers by applying a discretized form of the Green-Gauss theorem. This scheme reconstructs exact values of a linear function at a node from surrounding cell-centered values on arbitrary unstructured meshes by solving a constrained minimization problem, preserving a second-order spatial accuracy. The inviscid flux vector **F** appearing in (1) is evaluated by Advection Upstream Splitting Method[10] (AUSM). FLUENT utilizes an all-speed AUSM+ scheme[11] based on the low Mach number preconditioning. The coupled set of governing equations (1) is discretized in time using an implicit time-marching algorithm. In the implicit scheme, an Euler implicit discretization in time is combined with a Newton-type linearization of the fluxes to produce a linearized system in delta form[12]. The system is solved using Incomplete Lower Upper factorization (ILU) in conjunction with an algebraic multigrid (AMG) method[4, 13] adapted for coupled sets of equations. Time marching proceeds until a steady-state solution is reached.

3. Test cases

3.1 Axisymmetric Mach 29 flow over a sphere

Steady-state numerical simulation of Mach 29 flow past a sphere with the diameter 60.96 mm is considered. The main focus here is predicting flow conditions in the stagnation region, thus only the front half on the sphere is modeled. Flow is assumed to be axisymmetric and laminar. Freestream static pressure and temperature are 12.21 Pa and 196.7 K, respectively. Air is modeled as a reacting dissociated mixture of six species (N2, O2, O, N, NO, NO^+) in thermal and chemical non-equilibrium. Each species of the mixture is assumed to be an ideal gas with the molecular viscosity μ modeled as a function of temperature by three-coefficient Sutherland's viscosity law, thermal conductivity k defined using the kinetic theory formulation[14] and specific heat C_p is approximated using a piecewise-linear function. Specific heat of the mixture is computed as a mass fraction average of heat capacities of its species, and mixture thermal conductivity and molecular viscosity are computed based on kinetic theory[14]. The laminar finite-rate model[4] is applied to compute chemical source terms in the energy equation using Arrhenius expressions. The model is exact for laminar flames, but it ignores the effects of turbulent fluctuations. It is acceptable for combustion with relatively slow chemistry and small turbulent fluctuations, such as supersonic flames. Reaction system is defined by six dissociation equations,

$$\begin{array}{lll} O_2+M \Leftrightarrow 2O+M & N_2+M \Leftrightarrow 2N+M & NO+M \Leftrightarrow N+O+M \\ NO+O \Leftrightarrow O_2+N & N_2+O \Leftrightarrow NO+N & N+O \Leftrightarrow NO^{+}+e^{-} \end{array} \quad \textbf{(3)}$$

where M is the third body. Pressure far-field condition is used to simulate free-stream flow at the far-filed boundary, with free-stream Mach number and static conditions being specified. This non-reflecting boundary condition is based on the introduction of Riemann invariants (i.e., characteristic variables) for a one-dimensional flow normal to the boundary. Iso-thermal 1500 K boundary condition is applied at the sphere wall. Structured 2D mesh of 6400 quad cells is generated using the GAMBIT pre-processor[15]. The mesh is refined near the wall to resolve the laminar boundary layer. The solution is initialized with freestream values, chemical reactions turned on the beginning of simulation, and the solution is converged to the steady-state without first converging the no-chemistry case. Fig. 1 shows contours of Mach number, static pressure and temperature around the sphere. The shock ahead of the sphere is accurately captured. Distributions of normalized static temperature, density, and mass fraction of O_2, O and N_2 along the stagnation streamline are plotted in Fig. 2. Also shown in Fig. 2 are solutions computed by other researchers[16-17]. Values predicted by FLUENT 6.3 are in favorable agreement with previously published results.

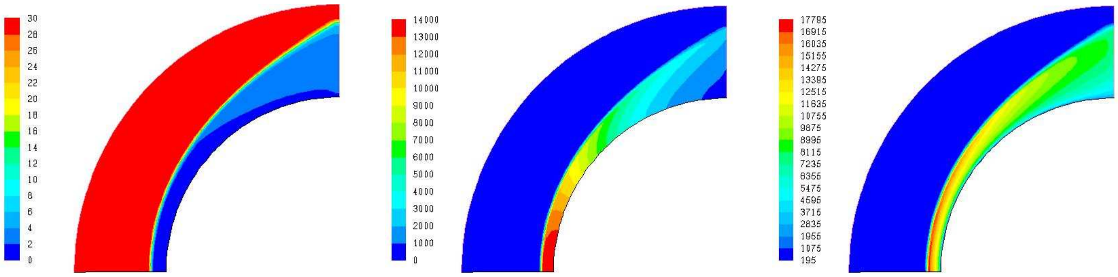

(a) (b) (c)

Figure 1: Contours of (a) Mach number, (b) static pressure, and (c) static temperature in Mach 29 flow over a sphere

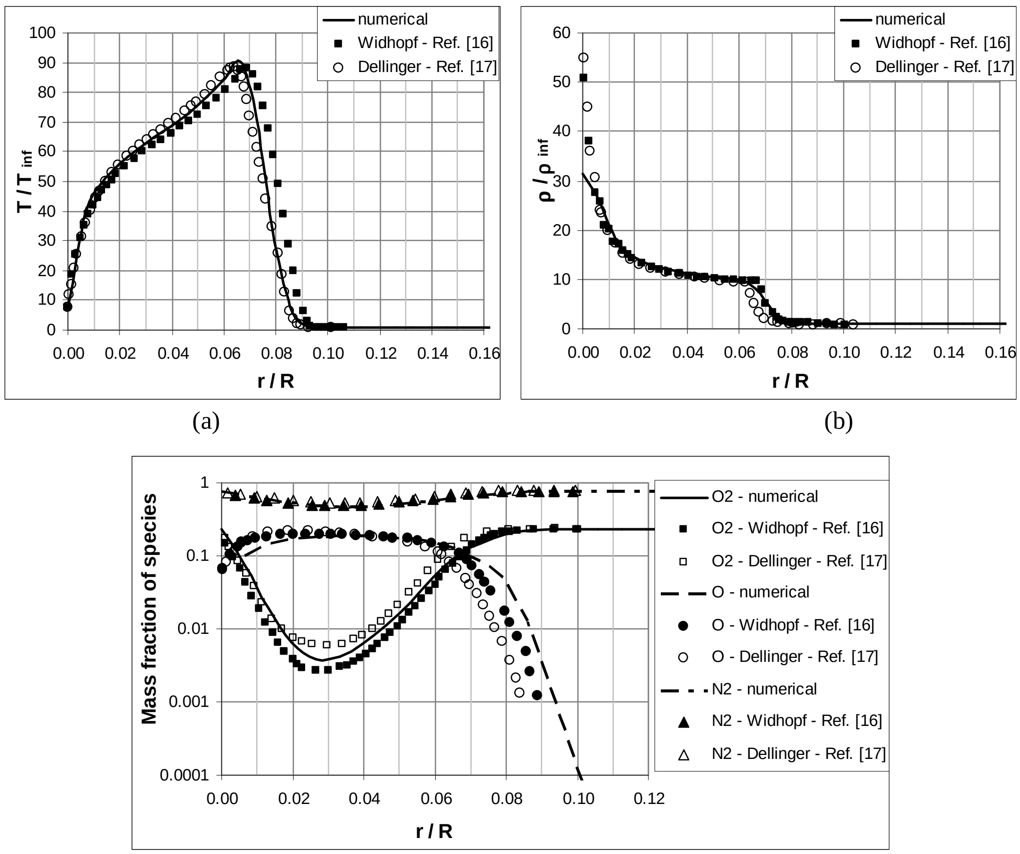

(a) (b)

(c)

Figure 2: Distributions of (a) normalized static temperature, (b) normalized density, and (c) mass fraction of O_2, O and N_2 along the stagnation streamline. Also shown are solutions of other researchers[16-17].

3.2 Axisymmetric Mach 9.85 flow over a hyperboloid flare

Axisymmetric hyperboloid flare in Mach 9.85 flow is studied in this test. The flare geometry is derived from the windward center line of Hermes 1.0 space plane[18, 19] at 30 deg angle of attack with 20 deg deflected body flap. Block-structured 2D mesh of 34,100 quad cells was created in the GAMBIT pre-processor[15]. Modeled geometry and computational domain with the mesh is shown in Fig. 3. The mesh is refined at the wall for adequate resolution of the laminar boundary layer. Freestream static pressure and temperature are 300 Pa and 514 K, respectively. Flow is considered to be laminar. Air is modeled as a reacting dissociated mixture of five species (N2, O2, O, N, NO) in thermal and chemical non-equilibrium. Each species of the mixture is assumed to be an ideal gas with the molecular viscosity μ and thermal conductivity k defined using the kinetic theory formulation[14], and specific heat C_p is modeled using a polynomial fit. Specific heat, thermal conductivity and molecular viscosity of the mixture are computed as discussed in Sec. 3.1. The laminar finite-rate model[4] (also discussed in Sec. 3.1) is applied. Reaction system is defined by first five dissociation equations in (3). Ionization processes are assumed to be negligible under current operating conditions. Flare and flap wall are taken to be iso-thermal with prescribed temperature of 300 K. Free-stream flow at the far-filed boundary is enforced by the pressure far-field condition. The outflow boundary is treated as a pressure outlet which uses specified static pressure and extrapolates all other flow variables from the interior of the domain if the flow is locally subsonic. In supersonic regions, all flow variables including static pressure are extrapolated from the interior. Fig. 4 shows contours of Mach number, static pressure and temperature around the flare. Numerical distributions of pressure coefficient C_p, and Stanton number St, are compared with experimental values[18] in Fig. 5. Numerical simulation accurately predicts the separation region (Fig. 6) and separation shock associated with the flow around the compression corner. Dip in St at around 0.09 m (Fig. 5b) reflects reduction in heat transfer from the fluid into the wall in the separation region. There is favorable agreement between C_p and St values predicted by FLUENT 6.3 and those of the test data[18].

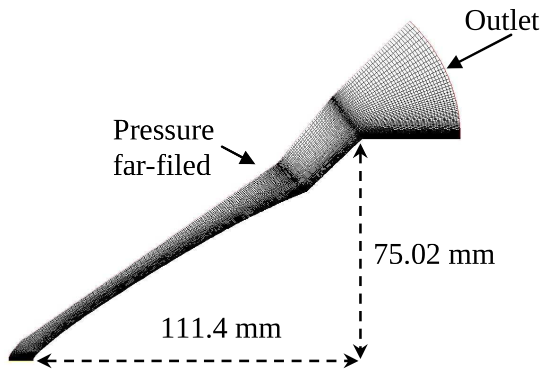

Figure 3: Hyperboloid flare geometry and computational mesh

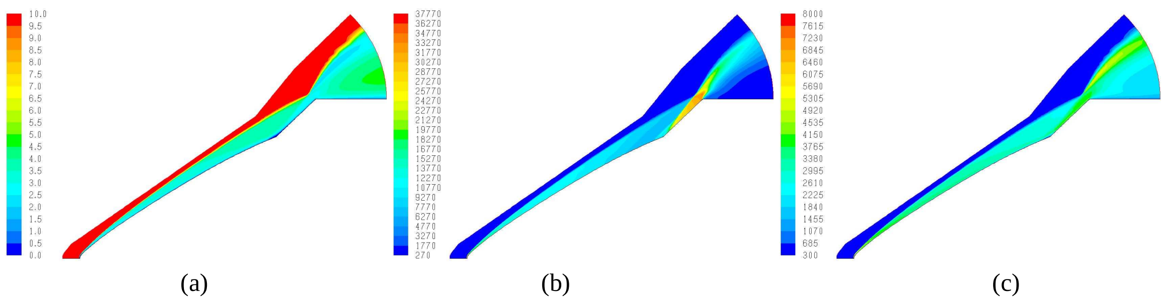

Figure 4: Contours of (a) Mach number, (b) static pressure, and (c) static temperature in Mach 9.85 flow over a hyperboloid flare

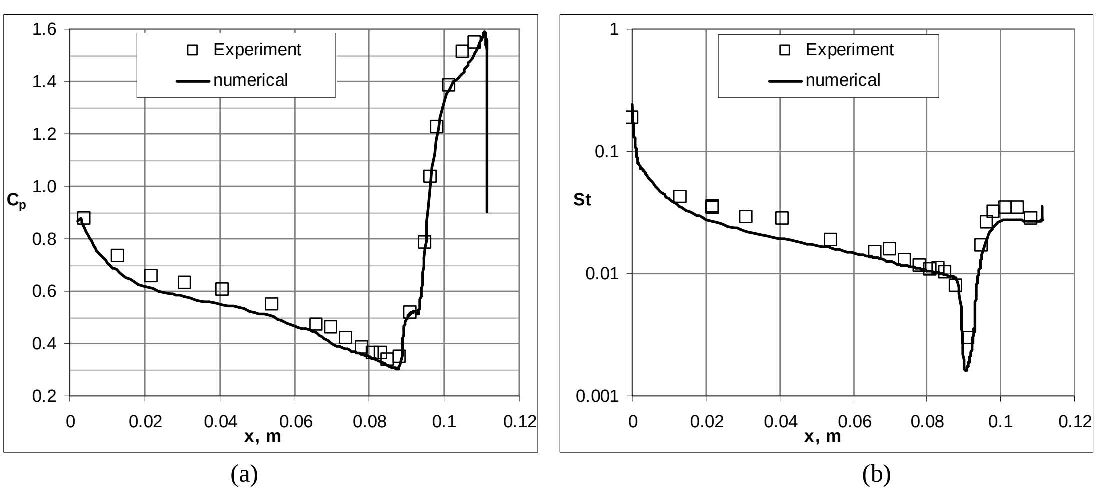

Figure 5: (a) pressure coefficient, and (b) Stanton number distribution along the flare and flap walls

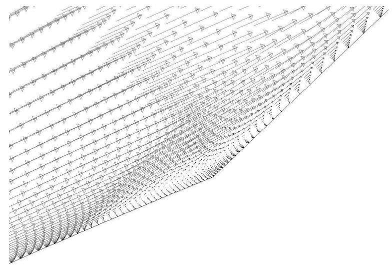

Figure 5: Velocity vector field at the compression corner between the flare and flap showing recirculation zone

3.3 Three-dimensional Mach 6 hypersonic missiles with aerospike

Missile model considered in this study correspond to the aerospiked missile geometries used in the experimental tests[20] (Fig. 6). The model consists of a 101.6 mm long cylindrical body with 101.6 mm diameter, and a 76.2 mm diameter hemispherical dome offset form the body with a 6.35 mm cylindrical extension of the same diameter. A 304.8 mm long aerospike tipped with 29.36 mm diameter aerodisc is mounted on the missile dome. Freestream conditions match those applied in Ref. 20: static pressure and temperature are 1951 Pa and 58.25 K, respectively, and Mach number is 6.06. The freestream Reynolds number at these conditions is 2.5×10^{7} per meter. The angle of attack (AOA) in the numerical study is 0 and 10 deg.

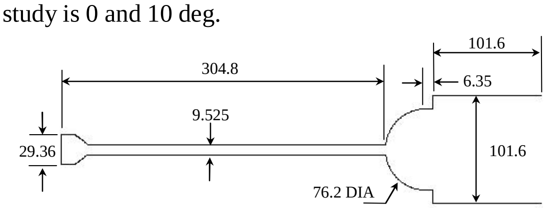

Figure 6: Aerospike-missile geometry. All dimensions are in millimeters.

Air is modeled as a single-species ideal gas. For the Mach number and operating conditions under consideration, real-gas thermodynamic non-equilibrium processes are not expected to have a strong effect on aerodynamic heating, and aerothermochemical model is not taken into account in the simulation. Kinetic theory formulation[14] is applied to define air viscosity μ, thermal conductivity k and specific heat C_p. The SST $k-\omega$ turbulence model[21] is employed to simulate turbulence effects. Pressure far-field boundary is used to prescribe free-stream Mach number and static conditions at infinity. The outflow boundary is treated as a pressure outlet. A 3D unstructured hexahedral computational mesh is generated using the GAMBIT pre-processor[15]. It contains a structured boundary layer type mesh around the aerospike and missile body fine enough to resolve the viscosity-affected near-wall region all the way to the laminar sublayer to ensure y^{+} in the wall-adjacent cell is on the order of one. The flow is assumed to be symmetric about $x-y$ coordinate plane, and only one-half of the model is included in the computational domain. The mesh is built for one-quarter of the model, and then copied to construct the mesh for half the model. The wake region is not considered in the numerical model since the study concentrates on predicting forces and thermal loads exerted on the missile dome. Fig. 7 shows close-up and full views of the computational mesh around one-quarter of the model.

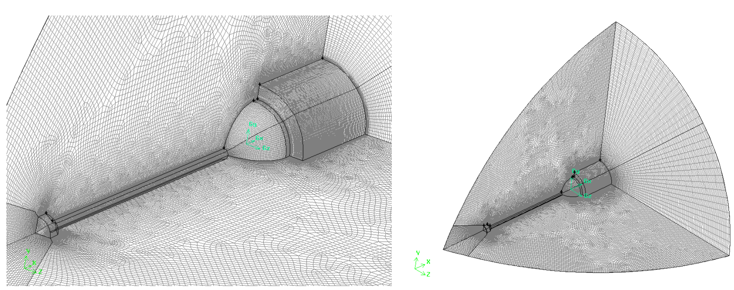

Figure 7: Computational mesh of the aerospike-missile geometry

The numerical solution is initialized from the free-stream flowfield, and then the full multigrid (FMG) initialization[4] is utilized to obtain the initial solution. FMG initialization is based on the full-approximation storage (FAS) multigrid technology[4, 22]. FMG procedure constructs several grid levels to combine groups of cells on the finer grid to form coarse grid cells. FAS multigrid cycle is applied on each level until a given order of residual reduction is obtained, then the solution is interpolated to the next finer grid level, and the FAS cycle is repeated again from the current level all the way down to the coarsest level. This process is continued until the finest grid level is reached. FMG initialization is relatively inexpensive since most of computational work is done on coarse levels, which allows to obtain a good initial solution that already recovers some flow physics. The solution is then iterated until the steady-state is reached. Fig. 8 shows contours of Mach number based on the local speed of sound at AOA = 0 deg with the aerospike (Fig. 8a) and without it (Fig. 8b). There is a well-resolved detached shock in front of the missile dome in the spike-off configuration. A separation region caused by the collar of the missile body is observed in Fig. 8b. The aerospike moves the bow shock away from the missile dome, which is fully enclosed in the spike-induced subsonic separation region (Fig. 8a). These observations are consistent with those reported experimentally[20]. Contours of static temperature for spike-on and spike-off configurations are displayed in Fig. 8c-d. It shows lower temperatures around the missile dome protected by the spike which results in lower heat load on the dome. Fig. 9a compares pressure on the missile dome normalized by the freestream static pressure for the two configurations with and without the aerospike, plotted versus the arc length measured along the dome surface starting from its foremost point. The flow is effectively axisymmetric at AOA = 0 deg, and only a single line distribution is shown. Aerospike reduces the surface pressure by about a factor of 3 at the base of the dome, and by as much as a factor of 15 at the spike root. Experimental values are also shown in Fig. 9a. There is a favorable agreement between numerical results and test data[20]. Ref. 20 does not provide heat transfer data, and instead presents surface temperature-rise data, which proves to be problematic to convert to appropriate thermal boundary conditions for the numerical simulation. Thus, adiabatic boundary conditions for aerospike and missile surfaces are chosen in the simulation, and only numerical values of surface temperatures are reported. Fig. 9b compares missile dome surface temperature normalized by freestream static temperature for spike-on vs. spike-off configurations, plotted along the same line as the pressure distribution. Aerospike decreases the dome surface temperature by about 10%. Fig. 10 shows contours of local Mach number and static temperature around the missile with and without the spike at AOA = 10 deg. The benefit of the areospike is limited only to the leeward side of the missile dome, which is enveloped in the spike separation region behind the separation shock. Fig. 11 and 12 quantify the aerospike effect by plotting normalized surface pressure and temperature along the leeward and windward sides of the dome. The windward side of the dome is no longer protected by the spike. The separation shock below the spike impinges on the dome as shown in Fig. 13, which forces an abrupt increase of surface pressure at the impingement point. The location of the impingement point can clearly be seen in Fig. 11b at around s = 0.47 inches, where the pressure distributions has a sharp peak. The experimental study[20] reported that pressure at the impingement point exceeded the maximum allowable limit of pressure sensors used in the tests, and did not provide data at this location. Numerical values of surface pressure reported in Fig. 11 are in favorable agreement with test data[20].

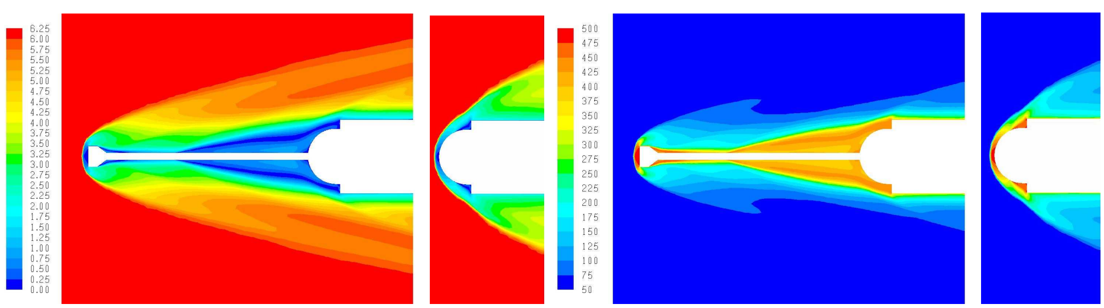

(a) (b) (c) (d)

Figure 8: Contours of (a-b) local Mach number, and (c-d) static temperature around the missile at AOA = 0 deg. (a, c) configuration with aerospike/aerodisc, and (b, d) missile without the spike protection.

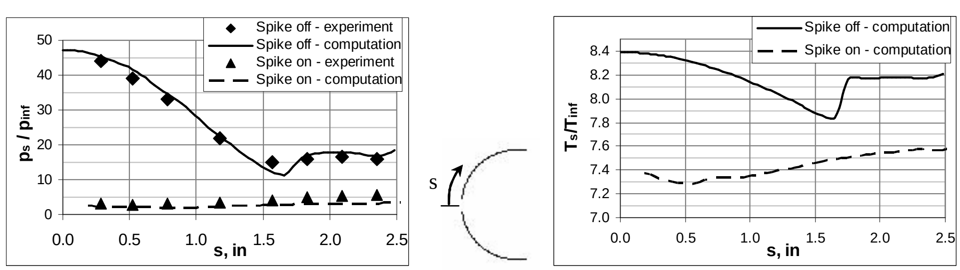

(a) (b)

Figure 9: (a) pressure, and (b) temperature distribution at AOA = 0 deg along the missile dome surface with and without aerospike protection

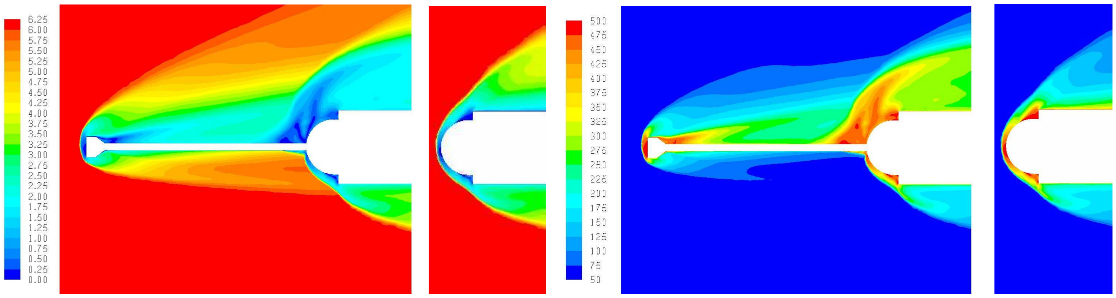

(a) (b) (c) (d)

Figure 10: Contours of (a-b) local Mach number, and (c-d) static temperature around the missile at AOA = 10 deg. (a, c) configuration with aerospike/aerodisc, and (b, d) missile without the spike protection.

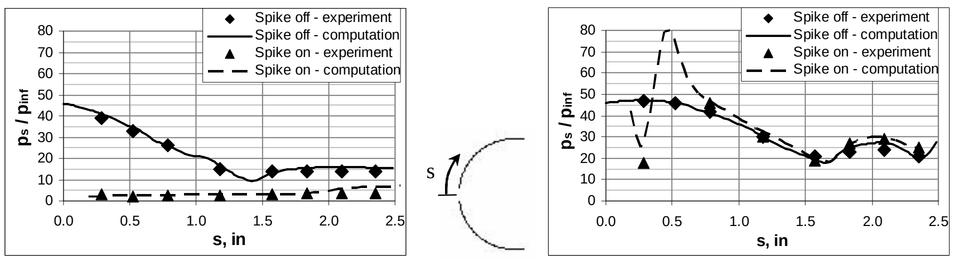

(a) (b)

Figure 11: Pressure distribution at AOA = 10 deg along (a) leeward, and (b) windward side of the missile dome with and without aerospike protection

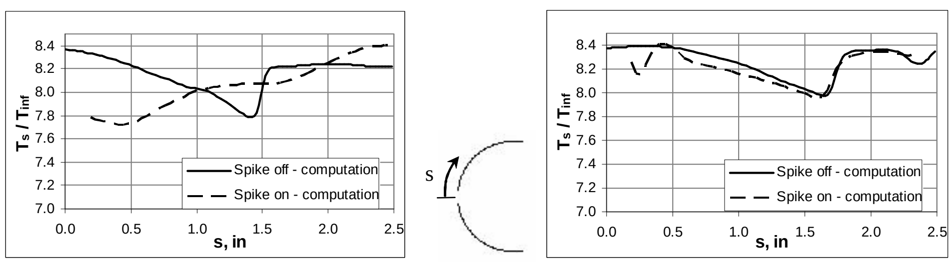

(a) (b)

Figure 12: Temperature distribution at AOA = 10 deg along (a) leeward, and (b) windward side of the missile dome with and without aerospike protection

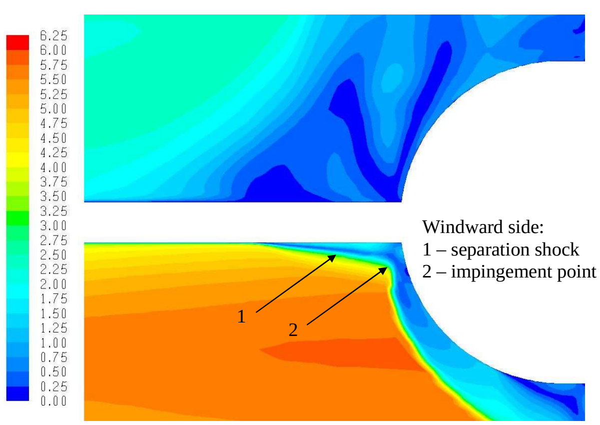

Figure 13: Enlarged view of the local Mach number contour map around the missile with aerospike at AOA = 10 deg showing the separation shock and its impingement point on the dome at the windward side.

4. Conclusion

The problem of external hypersonic flows is studied computationally using the density-based coupled solver (DBCS) implemented in the general purpose CFD code FLUENT, version 6.3. Results of numerical tests show that DBCS proves to be a robust and efficient method that can adequately resolve the physics and capture all essential features of the flowfield including shock – shock and shock – boundary layer interactions. Thermochemical dissociation effects are accounted for by the laminar finite-rate formulation for reaction modeling. Observations of numerical simulations are in line with those reported in prior experimental works.

5. Acknowledgements

The authors thank Laith Zori of ANSYS - Fluent Inc. and Patxi Gil Ramírez of ANSYS - Fluent France for providing initial case set-up and guidance for the hypersonic sphere problem.

References

[1] Murphy, T. K. S., (editor). Computational methods in hypersonic aerodynamics. Spirnger, first edition, 2007.
[2] Anderson, J. D. Hypersonic and high temperature gas dynamics. American Institute of Aeronautics and Astronautics, second edition, 2002.
[3] Ivanov, M.S., and Gimelshein, S.F. Computational hypersonic rarefied flows. *Annual review of fluid mechanics*, 30: 469-505, 1998.
[4] FLUENT 6.3 User's Guide, Fluent Inc., Lebanon, NH 03766, USA.
[5] Weiss, J. M., and Smith, W. A. Preconditioning applied to variable and constant density flows. *AIAA Journal*, 33(11):2050-2057, 1995.
[6] Barth, T. J., and D. Jespersen, D. The design and application of upwind schemes on unstructured meshes. *Technical Report AIAA-89-0366*, AIAA 27th Aerospace Sciences Meeting, Reno, Nevada, 1989.
[7] Kim, S.-E., Makarov, B., and Caraeni, D. A multi-dimensional linear reconstruction scheme for arbitrary unstructured grids. *AIAA Paper 2003-3990*.
[8] Holmes, D. G., and Connell, S. D. Solution of the 2D Navier-Stokes equations on unstructured adaptive grids. *AIAA Paper 89-1392*.
[9] Rauch, R. D., Batira, J. T., and Yang, N. T. Y. Spatial adaption procedures on unstructured meshes for accurate unsteady aerodynamic flow computations. *AIAA Paper 91-1106*.
[10] Liou, M. S., and Steffen, C. J., Jr. A new flux splitting scheme. *Journal of Computational Physics*, 107(1):23-39, 1993.
[11] Liou, M. S. A sequel to AUSM: AUSM+. *Journal of Computational Physics*, 129:364-382, 1996.
[12] Weiss, J. M., Maruszewski, J. P., and W. A. Smith. Implicit solution of the Navier-Stokes equations on unstructured meshes. *Technical Report AIAA-97-2103*, 13th AIAA CFD Conference, Snowmass, CO, 1997.
[13] Hutchinson, B. R., and Raithby, G. D. A multigrid method based on the additive correction strategy. *Numerical Heat Transfer*, 9:511-537, 1986.
[14] Hirschfelder, J. O., Curtiss, C. F., and Bird, R. B. Molecular theory of gases and liquids. John Wiley & Sons, New York, 1954.
[15] Gambit 2.3 User's Guide, Fluent Inc., Lebanon, NH 03766, USA.
[16] Widhopf, G. F., and Wang, J. C. T. A TVD finite-volume technique for nonequilibrium chemically reacting flows. *AIAA Paper 1988-2711*.
[17] Dellinger, T. C. Computation of nonequilibrium merged stagnation shock layers by successive accelerated replacement. AIAA Journal, 9(2):262-269, 1971.
[18] Sagnier, Ph., Joly, V, and Marmignon, C. Analysis of nonequilibrium flow calculations and experimental results around a Hyperboloid-flare configuration. *Proceedings of the 2nd European Symposium on Aerodynamics for Space Vehicles, ESA SP-367*, 1995
[19] Durand, G., Coron, F., Drouin, N., Duffa, G., Desmeuzes, C, Devezeaux, D., and Hugues, E. Reentry flight predictions around a hyperboloid-flare configuration by means of non-equilibrium real gas Navier-Stokes simulation. *AIAA Paper 1994-1824*.
[20] Huebner, D. L., Mitchell, A. M., and Boudreaux, E. J. Experimental results on the feasibility of an aerospike for hypersonic missiles. *AIAA Paper 95-0737*.
[21] Menter, F. R. Two-equation eddy-viscosity turbulence models for engineering applications. *AIAA Journal*, 32(8): 1598-1605, 1994.
[22] Brandt, A. Multi-level adaptive computations in fluid dynamics. *AIAA Paper 79-1455*.

This page has been purposedly left blank